

Parameter-Space Survey of Linear G-Mode and Interchange in Extended Magnetohydrodynamics

E. C. Howell¹ and C. R. Sovinec

**University of Wisconsin-Madison
Center for Plasma Theory and Computation
Report UW-CPTC 17-5 (revised)**

September 14, 2017

This article has been accepted for publication in the Physics of Plasmas, <http://aip.scitation.org/toc/php/current>, for publication in the category of basic plasma phenomena, waves, and instabilities.

NOTICE

This report was prepared as an account of work sponsored by an agency of the United States Government. Neither the United States Government, nor any of their employees, makes any warranty, express or implied, or assumes any legal liability for the accuracy, completeness, or usefulness of any information, apparatus, product, or process disclosed, or represents that its use would not infringe privately owned rights. Reference herein to any specific commercial product, process, or service by trade name, trademark, manufacturer, or otherwise does not necessarily constitute or imply its endorsement, recommendation, or favoring by the United States Government or any agency thereof. The views and opinions of authors expressed herein do not necessarily state or reflect those of the United States Government or any agency thereof.

¹Presently at Auburn University, Auburn, AL 36849.

Parameter-Space Survey of Linear G-mode and Interchange in Extended Magnetohydrodynamics

E. C. Howell^{1, a)} and C. R. Sovinec^{1, b)}

Department of Engineering Physics, University of Wisconsin-Madison, 1500 Engineering Drive, Madison, WI 53706-1609, USA

(Dated: 11 September 2017)

The extended magnetohydrodynamic stability of interchange modes is studied in two configurations. In slab geometry, a local dispersion relation for the gravitational interchange mode (g-mode) with three different extensions of the MHD model [P. Zhu, *et al.*, Phys. Rev. Lett. **101**, 085005 (2008)] is analyzed. Our results delineate where drifts stabilize the g-mode with gyroviscosity alone and with a two-fluid Ohm's law alone. Including the two-fluid Ohm's law produces an ion drift wave that interacts with the g-mode. This interaction gives rise to a second instability at finite k_y . A second instability is also observed in numerical extended MHD computations of linear interchange in cylindrical screw-pinch equilibria, the second configuration. Particularly with incomplete models, this mode limits the regions of stability for physically realistic conditions. However, applying a consistent two-temperature extended MHD model that includes the diamagnetic heat flux density (\bar{q}_*) makes the onset of the second mode occur at larger Hall parameter. For conditions relevant to the SSPX experiment [E.B. Hooper, Plasma Phys. Controlled Fusion **54**, 113001 (2012)], significant stabilization is observed for Suydam parameters as large as unity ($D_s \lesssim 1$).

I. INTRODUCTION

Extended-MHD models are extensions of magnetohydrodynamics (MHD) that bridge the gap between MHD and kinetic models. The macroscopic evolution of magnetically confined plasma is most accurately described in six-dimensional phase space using a kinetic model. However, kinetic models can be difficult to analyze, and at present, long-time kinetic simulations of macroscopic dynamics are not feasible. Resistive MHD treats the plasma as a fluid in three-dimensional physical space, and it is frequently used to model long-time dynamics. MHD represents the limit of vanishing particle Larmor radii and neglects a number of physical effects that are relevant to high-temperature plasmas. Extended MHD models augment resistive MHD with some of the important high-temperature effects while retaining the convenience of fluid models.¹ However, as we emphasize in this work, incomplete versions of extended MHD pose a risk of distorting physical effects and introducing unphysical effects that would not occur in kinetic treatments or self-consistent extended MHD models.

Drift stabilization of interchange modes is one area where the additional effects represented in extended MHD are important. Interchange is a class of pressure-driven modes that are unstable in regions where the magnetic field curvature is concave towards regions of high pressure. Interchanging two adjacent flux tubes in these regions can access a lower energy state, hence the unstable behavior.² Electron and ion diamagnetic effects introduce drifts which alter the phase relations among

the responses that characterize interchange modes. This can enhance stability with respect to interchange when the drifts are sufficiently large.

The gravitational interchange mode (g-mode) is useful for studying drift stabilization of interchange modes. The g-mode analysis introduces a fictitious gravity to represent the interaction of pressure and field-line curvature in simple slab configurations. Rosenbluth, *et al.* applied kinetic analysis to this configuration to show that drift effects stabilize the g-mode when the drift frequency exceeds twice the MHD growth rate: $|\omega_*| > 2\gamma_{mhd}$.³ Roberts and Taylor reproduced the drift stabilization using a two-fluid model⁴ that can be viewed as a precursor to extended MHD.^{1,5} Later, Ferraro and Jardin generalized the g-mode analysis to include finite compressibility,⁶ and Zhu, *et al.* showed that complete stabilization of the g-mode can fail at finite β -values in a reduced fluid model that includes ion gyroviscosity but uses the MHD Ohm's law.⁷ More recently, Goto *et al.* showed that stabilization can also fail in the reduced model that uses the two-fluid Ohm's law but neglects ion gyroviscosity.⁸

The g-mode analysis presented here examines the behavior of Zhu's extended MHD system as the normalized gravitational drift frequency is scanned in reduced and complete models. A second instability at large normalized drift frequency is found in models with the Hall term in Ohm's law. The full extended MHD system with the Hall term and ion gyroviscosity also exhibits additional instabilities. Our analysis shows that the second instability arises due to the interaction between an ion drift wave and the stabilized g-mode. Additional unstable modes occur in conditions outside the validity of the extended MHD model, but they may be a concern for macroscopic modeling with this system.

There are regimes where coupling between the g-mode and other waves also leads to instabilities. A physically

^{a)}Presently at Auburn Univ., Auburn, AL 36849, USA; Electronic mail: ech0039@auburn.edu

^{b)}Corresponding author: csovinec@wisc.edu

relevant example, where gravity is a proxy for physical acceleration, occurs in laser plasma and magnetospheric releases.⁹ Huba, Hassam, and Lyon examine this behavior in Refs. 10 and 11 for conditions where the ion Larmor radius is larger than the scale of the density gradient. In this limit the ions are not magnetized, and an extended MHD model that includes the Hall term but neglects ion gyroviscosity is appropriate. In these conditions, coupling between the magnetosonic wave and the g-mode produces an instability that differs from the second instability studied here, which arises due to coupling between an ion drift wave and the g-mode. The ordering used by Zhu, *et al.*, and again in the present work, assumes that the ion gyroradius is small relative to equilibrium length-scales. The magnetoacoustic branch is factored-out of the dispersion relation, which precludes the large Larmor radius instability in our g-mode analysis.

The relation between our g-mode analysis and recent work by Ito and Miura, Ref. 12, deserves special mention. There are substantial parallels with respect to examining the predictions of MHD models that are extended by gyroviscosity alone, by a two-fluid Ohm's law alone, and by both effects. This framework follows from the study by Zhu, *et al.*, Ref. 7. As in the results presented in Section III, Ito and Miura find conditions where drift stabilization is and is not possible in the models and also note the existence of additional instabilities in some conditions. However, we work with normalized equations and the simpler profiles of Ref. 7, and we additionally apply asymptotic analysis, which all help elucidate the underlying physical dependencies. We also place more emphasis on the origins of the second instability that arises in models with a two-fluid Ohm's law.

Our study was initially motivated by an interest¹³ in interchange modes in the Sustained Spheromak Physics Experiment (SSPX).^{14,15} Thus, we also consider drift stabilization of interchange in cylindrical screw-pinch equilibria with parameters based on SSPX. Jardin first used this class of equilibria to map out the ideal stability boundaries of spheromaks.¹⁶ He showed that these equilibria reproduce the stability properties of toroidal equilibria for toroidal mode numbers $n \neq 1$. DeLucia, *et al.* used these model equilibria to study resistive interchange modes in spheromaks.¹⁷ They also present the first study of drift effects on interchange modes in spheromaks and find stabilization of the resistive interchange mode at sufficiently large ion skin depth in a model with cold ions. Hammet and Tang applied a kinetic model to study interchange modes in these equilibria and showed that kinetic effects greatly increase the stability limits of ideal interchange modes.¹⁸ We note that Hammet and Tang applied an ordering that removes drift waves from the system.

The cylindrical computations presented here find a second instability that has both similarities and differences to the second instability of the slab g-mode analysis. Relative to single-temperature predictions, two-temperature modeling with diamagnetic heat-flux density puts the onset of the second mode at larger values of the Hall param-

eter. Another recent study¹⁹ of cylindrical interchange considers the qualitatively different perpendicular conductive heat-flux density for stellarator profiles but does not address diamagnetic heat-flux density that proves important in our screw-pinch computations. The sensitivity of this second instability to which terms are included in both the g-mode and the screw-pinch results highlights the importance of using a self-consistent model.

The remaining sections of this paper are organized in the following manner: Section II discusses the extended MHD model considered in this work. The analysis of Zhu's local g-mode dispersion relation is presented in Section III. Section IV presents a numerical study of interchange modes in our model spheromak equilibria geometry. We conclude with a discussion of our results in Section V.

II. EXTENDED MHD MODEL

We consider an extended MHD model that is based on Braginskii's equations²⁰

$$\frac{\partial n}{\partial t} + \vec{V} \cdot \nabla n = -n \nabla \cdot \vec{V} \quad (1)$$

$$\rho \left(\frac{\partial \vec{V}}{\partial t} + \vec{V} \cdot \nabla \vec{V} \right) = \vec{J} \times \vec{B} - \nabla p - \nabla \cdot \vec{\pi}_i + \rho \vec{g} \quad (2)$$

$$\frac{n}{\gamma_s - 1} \left(\frac{\partial T_s}{\partial t} + \vec{V}_s \cdot \nabla T_s \right) = -p_s \nabla \cdot \vec{V}_s - \nabla \cdot \vec{q}_s \quad (3)$$

$$\nabla \times \vec{B} = \mu_0 \vec{J} \quad (4)$$

$$\nabla \cdot \vec{B} = 0 \quad (5)$$

$$\frac{\partial \vec{E}}{\partial t} = -\nabla \times \vec{E} \quad (6)$$

$$\vec{E} = -\vec{V} \times \vec{B} + \eta \vec{J} + \frac{1}{ne} \left(\vec{J} \times \vec{B} - \nabla p_e \right). \quad (7)$$

Equations 1-2 are the continuity and momentum equations for the bulk fluid. Here n is the number density (quasi-neutrality is assumed), m is the effective particle mass ($m_i + m_e$), \vec{V} is the center of mass flow velocity, $\rho = nm$ is the mass density, $p = p_i + p_e$ is the total pressure, $\vec{\pi}_i$ is the ion stress tensor, and $\rho \vec{g}$ is the force density due to gravity. Equation 3 is the temperature evolution equation for each species. Here γ_s is the ratio of specific heats, and \vec{q}_s is the heat flux density. Equations 4-6 are Ampere's law, the magnetic divergence constraint, and Faraday's Law. Equation 7 is the two-fluid Ohm's law and represents the electron momentum equation, where η is the electrical resistivity. The first two terms on the right side are the standard MHD Ohm's law. The Hall ($\vec{J} \times \vec{B}/ne$) and electron pressure-gradient ($\nabla p_e/ne$) terms represent two-fluid corrections to MHD. We note that Braginskii's derivation assumes that effective collisional mean-free-paths are small relative to spatial scales L and that flows are of the same

order as the ion thermal velocity v_{thi} , i.e. the ‘‘MHD ordering.’’²¹ Neither approximation is representative of high-temperature magnetic-confinement conditions, but the system does represent effects that are first-order in $v_{thi}/L\Omega_i$, where Ω_i is the ion cyclotron frequency.

The ion gyroviscous stress tensor appears in Equation (2) as part of $\vec{\pi}_i$. It represents the first-order corrections due to ion finite Larmor radius (FLR) effects and is given by the expression

$$\vec{\pi}_g = \frac{nT_i}{4\Omega_i} \left[\hat{b} \times \vec{W} \cdot \left(\vec{I} + 3\hat{b}\hat{b} \right) - \left(\vec{I} + 3\hat{b}\hat{b} \right) \cdot \vec{W} \times \hat{b} \right], \quad (8)$$

where \vec{W} is the traceless rate of strain tensor

$$\vec{W} = \nabla \vec{V} + (\nabla \vec{V})^\top - \frac{2}{3} \vec{I} \nabla \cdot \vec{V}, \quad (9)$$

\vec{I} is identity tensor, and \hat{b} is the direction of the magnetic field. With the exception of noted computations in Section IV C and the modeling presented in Section IV D, we assume that $T_i = T_e$.

The NIMROD^{22,23} code is used in Section IV to evolve Equations 1-7. These calculations include a dissipative isotropic stress, $-\rho\nu\vec{W}$, in $\vec{\pi}_i$. Artificial particle diffusivity and hyper-diffusivity ($\nabla \cdot (D\nabla n - D_h\nabla^2\nabla n)$) are also included in Equation 1 to aid the numerics by smoothing small-scale density fluctuations. NIMROD does not solve the magnetic divergence constraint explicitly; instead, a magnetic divergence diffusivity ($\chi_B\nabla\nabla \cdot \vec{B}$) is added to the right side of Equation 6 to maintain low divergence error with high-order representations.²²

In this work, we consider the consequences of using simplified versions of the extended MHD system of equations. The simplest is the MHD model, which neglects ion gyroviscosity and the two-fluid terms in Ohm’s law and is consistent at zeroth order in $v_{thi}/L\Omega_i$. The ‘‘gyroviscous model’’ includes ion gyroviscosity in the momentum equation but is otherwise identical to the MHD model. The ‘‘two-fluid model’’ neglects ion gyroviscosity but includes the Hall and electron pressure gradient terms in Ohm’s law. When applied to conditions without a temperature gradient, and for isothermal dynamics, it is equivalent to the large Larmor radius model of Ref. 11. The full extended MHD model includes both ion gyroviscosity and the two-fluid Ohm’s law. Zhu, *et al.* thoroughly analyzes the g-mode in the gyroviscous model and only briefly comments on behavior with the two-fluid and full models, noting that there are cases where stabilization may fail.⁷ A central contribution of the present work is to consider the stability predictions of these models in greater detail. For completeness, we also consider the gyroviscous model.

III. LOCAL ANALYSIS OF THE GRAVITATIONAL INTERCHANGE

In this section we use the gravitational interchange mode as a model for interchange stability in magnetically confined plasma. The analysis uses the local dispersion relation derived by Zhu, *et al.* for the g-mode in a shearless slab configuration.⁷ Zhu considers the static equilibrium described by

$$\vec{V} = 0 \quad (10)$$

$$\vec{B} = B\hat{e}_z \quad (11)$$

$$\frac{d}{dx} \left(p + \frac{B^2}{2\mu_0} \right) = \rho g \quad (12)$$

$$neE_x = \frac{d}{dx} p_i - \rho g, \quad (13)$$

where gravity points in the x -direction and is balanced by gradients in the pressure and magnetic field. Equilibrium quantities only vary in the x -direction.

The dispersion relation is derived using the extended MHD model (Equations 1-7). The derivation neglects dissipative effects, i.e. $\eta = \nu = \vec{q} = 0$, but retains the ion gyroviscous stress and the two-fluid terms in Ohm’s law. Perturbed quantities vary as $\tilde{f} = \tilde{f}(x) e^{ik_y y - i\omega t}$. The model uses the ordering $k_y L \sim \epsilon^{-1}$, $k_y r_i \sim 1$, and $\tilde{v}_y \sim \epsilon \tilde{v}_x$ where $\epsilon \ll 1$ is a small parameter, L is the equilibrium gradient scale length, and $r_i^2 = p_i / (\rho\Omega_i^2)$ is the square of the ion Larmor radius. Formally, extended MHD is only physically valid for $k_y r_i \ll 1$, but the ordering $k_y r_i \sim 1$ permits the study of the extended MHD model at all values of $k_y r_i$.

Our normalized form of Zhu’s g-mode dispersion relation is

$$(A_0 + A_2) X^3 + (X_{*1} + X_{*3}) X^2 + (\Upsilon_0 + \Upsilon_2) X + D_1 = 0 \quad (14)$$

$$A_0 = 1 + \gamma_s \beta \quad (15)$$

$$A_2 = \delta^2 \frac{\tau G^2 N}{4} \beta \quad (16)$$

$$X_{*1} = G (\delta [(1 + \gamma_s \beta) (1 + \beta) P + (2 + \gamma_s \beta) \tau \beta] + \lambda [1 + P - \gamma_s N]) \quad (17)$$

$$X_{*3} = -\delta^2 \lambda G^3 \frac{N^2}{4} \quad (18)$$

$$\Upsilon_0 = 1 + \gamma_s \beta + S \quad (19)$$

$$\Upsilon_2 = \delta \lambda G^2 [(1 + \beta) (P + 1) P - ((1 + \gamma_s \beta \tau) + (1 + \beta) \gamma_s P) N + (1 + P) \tau \beta] \quad (20)$$

$$D_1 = \lambda G (P - \gamma_s N), \quad (21)$$

where $X = \omega/\Gamma_M$ is the frequency normalized by $\Gamma_M = \sqrt{-\rho'g/\rho}$, the MHD growth rate in the $\beta, S \ll 1$ limit. We are interested in the case where the g-mode is MHD unstable and assume that Γ_M is real ($\rho'g < 0$). $G = \omega_g/\Gamma_M$ is the gravitational drift frequency, $\omega_g =$

$-k_y g / \Omega_i$, normalized by Γ_M . $P = \omega_{pi} / \omega_g$ and $N = \omega_{ni} / \omega_g = k_y^2 r_i^2 / G^2$ are the ion diamagnetic drift frequencies due to the ion pressure gradient, $\omega_{pi} = k_y p_i' / (\Omega_i \rho)$, and the ion density gradient, $\omega_{ni} = k_y p_i \rho' / (\Omega_i \rho^2)$, respectively, normalized by the gravitational drift frequency. The parameter $\tau = p_i / p$ is the ion pressure fraction, $\beta = \mu_0 p / B^2$, and $S = g^2 / (V_a^2 \Gamma_M^2) = \tau \beta / N$ scales the density variation with respect to the square of the Alfvén speed, $V_a^2 = B^2 / (\mu_0 \rho)$, and the gravitational acceleration. The markers λ and δ indicate contributions due to the two-fluid Ohm's law and gyroviscosity, respectively. The subscripts of the coefficients A_i , X_{*i} , Υ_i , and D_i indicate how the coefficients scale with G . For example, A_2 scales as G^2 .

The normalized parameters N , P , and S are properties of an equilibrium, and the relative strength of two-fluid and gyroviscous terms are represented by G . Increasing $|G|$ corresponds to increasing $k_y r_i$ for a given equilibrium profile. The limit of physical validity ($k_y^2 r_i^2 \ll 1$) expressed in dimensionless variables is $G^2 N \ll 1$. Since $r_i / L \sim \epsilon$ is implied in the ordering, the magnetoacoustic branch has been factored out of Equation 14 and is not represented in any results of Section III.

The normalized ion diamagnetic frequency N is positive for the unstable g-mode. Positive- N implies that the gravitational drift propagates in the ion-density-gradient diamagnetic direction, and waves with frequencies proportional to $+$ ($-$) G propagate in the ion (electron) diamagnetic direction. The magnitudes of P and N are determined by MHD force balance and the ion pressure fraction τ .

Equation 14 is a cubic polynomial with real coefficients. It always has at least one real root. The system is stable if there are three real roots. Otherwise, two roots are complex conjugates, and the system is unstable. One of the complex conjugates is a growing unstable mode, and the other is a damped stable mode. The growing and damped modes have the same real frequency and propagate in the same direction.

In Section III A a perturbative expansion is used to evaluate the roots in the small- $|G|$ limit. The method of dominant balance is used in the large- $|G|$ limit, where the scaling $X \sim O(G^n)$ is assumed. The exponent n is chosen such the highest order terms in Equation 14 balance. The resulting balance is used to calculate the asymptotic behavior of X . The roots of Equation 14 are calculated numerically for arbitrary G in Sections III B-III D.

A. Small G Perturbation Theory

The roots of Equation 14 in the small- $|G|$ limit are found using a perturbative expansion. The complex frequency X and Equation 14 are expanded into terms of order $|G|^n$. This expansion produces a hierarchy of equations. The three lowest-order equations are:

$$|G|^0 : A_0 X_0^3 + \Upsilon_0 X_0 = 0 \quad (22)$$

$$|G|^1 : X_1 = -\frac{D_1 + X_{*1} X_0^2}{3X_0^2 A_0 + \Upsilon_0} \quad (23)$$

$$|G|^2 : X_2 = \frac{-X_0}{3X_0^2 A_0 + \Upsilon_0} \times (A_2 X_0^2 + 3X_1^2 A_0 + 2X_{*1} X_1 + \Upsilon_2). \quad (24)$$

Equation 22 has three solutions $X_0 = 0$ and $X_0 = \pm i \sqrt{\Upsilon_0 / A_0}$. Inserting $X_0 = 0$ into Equations 23-24 produces the solution

$$X = -D_1 / \Upsilon_0 + O(|G|^3). \quad (25)$$

Equation 25 describes a stable ion drift wave. Its direction of propagation is determined by the sign of D_1 .

The two roots $X_0 = \pm i \sqrt{\Upsilon_0 / A_0}$ are the unstable g-mode and its corresponding damped complex conjugate. Inserting X_0 into Equations 23-24 produces the solution

$$X = Y_1 \pm i \sqrt{\frac{\Upsilon_0}{A_0}} \left[1 + \frac{1}{2\Upsilon_0} \left(3Y_1^2 A_0 + 2X_{*1} Y_1 + \Upsilon_2 - \frac{A_2}{A_0} \Upsilon_0 \right) \right] + O(|G|^3) \quad (26)$$

$$Y_1 = \frac{A_0 D_1 - X_{*1} \Upsilon_0}{2\Upsilon_0 A_0}. \quad (27)$$

Equations 26-27 describe the extended MHD modifications to the g-mode at small values of $|G|$. There are two effects. First, extended MHD imparts a finite real frequency of order G^1 . Second, extended MHD modifies the growth rate of the mode. This modification to the growth rate is of order G^2 . The sign of $3Y_1^2 A_0 + 2X_{*1} Y_1 + \Upsilon_2 - \frac{A_2}{A_0} \Upsilon_0$ determines if the extended MHD effects increase or decrease the growth rate at small- $|G|$. The Υ_2 and A_2 terms appear in the lowest-order correction to the growth rate. They are second-order in G and are normally neglected in derivations that assume a small ordering for the extended MHD effects. However, the lowest-order correction to the growth rate is at second order, and including these terms is necessary for consistency. Similarly, the term D_1 appears in the lowest-order corrections to both the real frequency and the growth rate. This term is linear in G , yet it is absent in derivations of the g-mode that predate Zhu, *et al.* Analysis of Equations 25 and 26 in the following sections augment our discussion of calculations with the systems for arbitrary G .

B. Gyroviscous g-mode Analysis

The dispersion relation for the gyroviscous model is found by setting $\delta = 1$ and $\lambda = 0$ in Equations 14 - 21. The dispersion relation in this case is

$$(A_0 + A_2)X^3 + X_{*g}X^2 + X\Upsilon_0 = 0 \quad (28)$$

$$A_0 = 1 + \gamma_s\beta \quad (29)$$

$$A_2 = \frac{\tau G^2 N}{4}\beta \quad (30)$$

$$X_{*g} = G[(1 + \gamma_s\beta)(1 + \beta)P + (2 + \gamma_s\beta)\tau\beta] \quad (31)$$

$$\Upsilon_0 = 1 + \gamma_s\beta + S. \quad (32)$$

There are three solutions to the cubic dispersion relation. The first solution is the zero-frequency mode $X = 0$. The other two solutions are found using the quadratic equation

$$X = \frac{1}{2A} \left(-X_{*g} \pm \sqrt{X_{*g}^2 - 4A\Upsilon_0} \right), \quad (33)$$

where $A = A_0 + A_2$. The two roots are real (indicating stability) if $X_{*g}^2 - 4A\Upsilon_0 \geq 0$, and they are complex (indicating instability) if $X_{*g}^2 - 4A\Upsilon_0 < 0$. The stability requirement that $X_{*g}^2 - 4A\Upsilon_0 \geq 0$ can be expressed as

$$G^2 \left[\frac{[(1 + \gamma_s\beta)(1 + \beta)P + (2 + \gamma_s\beta)\tau\beta]^2}{1 + \gamma_s\beta + S} - \tau N\beta \right] \geq 4(1 + \gamma_s\beta). \quad (34)$$

The inequality is never satisfied for real G if the term in brackets is negative, and stabilization does not occur. This equation is analogous to Equation 22 in Ref. 7 (and Equation 54 in Ref. 12), where the authors note that in the $\beta \rightarrow 0$ limit, the bracketed term is positive. In this limit gyroviscous stabilization always occurs at significantly large G . In Appendix A we show that the bracketed term in Equation 34 is also positive for $0 < N \leq P$. This condition corresponds to the situation where both ∇n and ∇T are anti-parallel to \vec{g} .

From Equation 33 we observe that X scales as G^{-1} in the limit that $|G| \gg 1$. Therefore, even in cases where stabilization is not possible, the asymptotic growth rate still goes to zero with G^{-1} .

In the limit of $|G| \ll 1$, the perturbative expansion from Section III A yields

$$X \approx \frac{-X_{*g}}{2(1 + \gamma_s\beta)} \pm i \sqrt{\frac{1 + \gamma_s\beta + S}{1 + \gamma_s\beta}} \left(1 - \frac{\tau\beta G^2 N}{8(1 + \gamma_s\beta)} - \frac{X_{*g}^2}{8(1 + \gamma_s\beta)(1 + \gamma_s\beta + S)} \right) + O(G^3). \quad (35)$$

At small values of $|G|$, the gyroviscous g-mode has a real frequency, and the mode propagates in a direction determined by the sign of X_{*g} . X_{*g} has the same sign as G for positive P , and the mode propagates in the electron

diamagnetic direction. The second and third terms in parentheses in Equation 35 are positive definite, indicating that gyroviscosity is stabilizing at small- $|G|$.

Figure 1 shows the numerically calculated frequencies for equilibrium parameters $\tau = 0.5$, $\beta = 0.1$, $P = 0.5$, $N = 0.025$, and $S = 2$, where the bracketed term in Equation 34 is positive, so stabilization is possible. There are three modes: the unstable branch of the g-mode (green), the stable branch (blue), and the trivial zero frequency mode (red). Initially the two branches of the g-mode have the same real frequency. The frequency is negative indicating that they propagate in the electron diamagnetic direction. Increasing G decreases the growth rate of the unstable branch, and stabilization is observed around $G \approx 5$. At the point of stabilization, the real frequencies of the two branches of the g-mode split. At sufficiently large G , beyond the range of the plot, both real frequencies asymptote to zero. However, at large G the model is not physically valid.

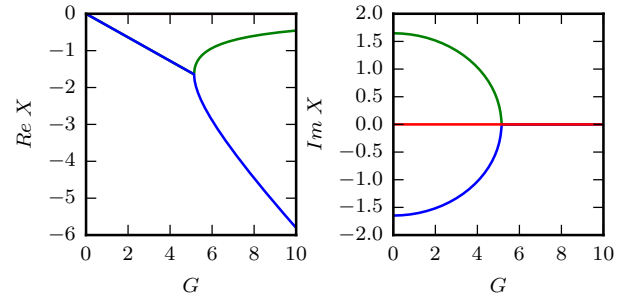


FIG. 1. Linear growth rates characteristic of the gyroviscous g-mode for conditions where the bracketed term in Equation 34 is positive. Initially both the unstable branch (green) and the stable branch (blue) have the same real frequency. After stabilization, the two modes have different real frequencies. Both branches eventually asymptote to zero at large- G (not shown).

Figure 2 shows the numerically calculated frequencies for a case that has $\tau = 0.5$, $\beta = 0.1$, $P = 1 \times 10^{-3}$, $N = 1$, and $S = 0.05$, where $X_{*g}^2 - 4A\Upsilon_0 < 0$ for all G^2 , hence an unstable mode for all G . Here, the growth rate of the unstable branch continuously decreases with increasing G and asymptotes to zero as G^{-1} . The real frequency of both branches of the g-mode are the same for all G . The frequency is again negative, indicating that the mode propagates in the electron direction. Initially, its magnitude increases with G , but it peaks at an intermediate value, and then it asymptotes to zero at the rate G^{-1} .

C. Two-Fluid g-mode Analysis

The dispersion relation for the two-fluid model is found by setting $\delta = 0$ and $\lambda = 1$ in Equations 14-21. The resulting dispersion relation is

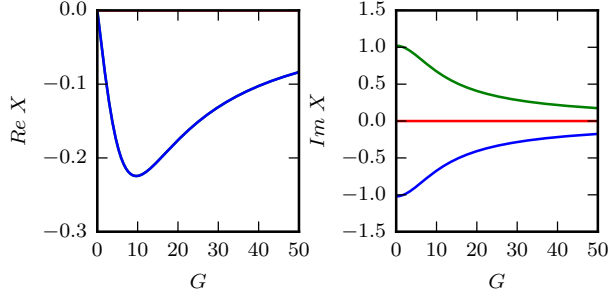


FIG. 2. Linear growth rates characteristic of the gyroviscous g-mode in conditions with $X_{*g}^2 - 4A\Upsilon_0 < 0$. Both branches of the g-mode have the same real frequency for all G . The real and imaginary frequencies asymptote to zero at large- G .

$$AX^3 + X_*X^2 + X\Upsilon_0 + D = 0 \quad (36)$$

$$A = 1 + \gamma_s\beta \quad (37)$$

$$X_* = G(1 + P - \gamma_s N) \quad (38)$$

$$\Upsilon_0 = 1 + \gamma_s\beta + S \quad (39)$$

$$D = G(P - \gamma_s N). \quad (40)$$

We set $\beta = 0$ in this system but allow for finite P and N . None of the terms containing β depend on G , and setting $\beta = 0$ does not change the qualitative behavior of the model. It effectively re-scales the coefficients in Equation 36. Additionally, β is small for most systems of interest, and neglecting it has a small quantitative effect. For simplicity, we also take the limit of $S = g\rho/V_A^2\rho' \rightarrow 0$. Thus, the model two-fluid g-mode dispersion relation that we analyze is

$$X^3 + X_*X^2 + X + D = 0 \quad (41)$$

$$X_* = G(1 + H) \quad (42)$$

$$D = GH. \quad (43)$$

Equation 41 only depends on the two parameters G and $H = P - \gamma_s N$. The parameter H is a normalized modified ion diamagnetic drift frequency. It is purely a function of equilibrium quantities, and in the cold-ion limit, where dropping ion-FLR effects is formally valid, $H = 0$. The condition $H = 0$ is also applicable to isothermal, $\gamma_s = 1$, dynamics in the absence of equilibrium temperature gradients.

A criterion for stability is found by considering the critical points of the polynomial $Q(X) = X^3 + X_*X^2 + X + D$. The critical points $x_a \leq x_b$ satisfy the condition $Q'(x_a) = Q'(x_b) = 0$. A necessary condition for stability is that x_a and x_b must both be real with $Q(x_a) \geq 0$ and $Q(x_b) \leq 0$. The direction of the inequalities results from the fact that the leading-order coefficient, A , is positive. If $x_a = x_b$ then stability requires $Q(x_a) = Q(x_b) = 0$. This stability criterion follows from the mean value

theorem and the requirement that $Q(X)$ has three real roots.

The critical points of $Q(X)$ are

$$x_{a,b} = \frac{-G(1+H)}{3} \pm \frac{1}{3}\sqrt{G^2(1+H)^2 - 3}. \quad (44)$$

Stability requires that the two critical points given in Equation 44 are real. It follows that a necessary (but not sufficient) condition for stability is

$$G^2(1+H)^2 \geq 3. \quad (45)$$

Equation 45 shows that conditions with either $H = -1$ or $G = 0$ are in the unstable regime.

We first use Equations 25-27 to understand the solutions to the two-fluid dispersion relation in the limit $|G| \ll 1$. In this model $\Upsilon_0 = A_0 = 1$, $\Upsilon_2 = 0$, $A_2 = 0$, $D_1 = GH$, and $X_{*1} = G(1+H)$. Inserting these relations into Equation 25 produces the stable drift wave $X = -GH$. The drift wave propagates in the electron diamagnetic direction when H is positive and in the ion direction when H is negative.

Evaluating Equations 26-27 for the two-fluid model produces $X = -G/2 \pm i[1 - G^2(1+4H)/8]$. The + solution is the unstable g-mode, and the - solution is the corresponding damped mode. Two-fluid effects reduce the growth rate of the unstable mode at small $|G|$ when $H > -1/4$ and increase it when $H < -1/4$. A higher-order perturbative expansion is required to evaluate the case $H = -1/4$. Both branches of the g-mode propagate in the electron diamagnetic direction.

We analyze the opposite limit of $|G| \gg 1$ by assuming that X scales as either G^1 or G^0 for $H \neq -1$. In the case that X scales as G^1 , the first two terms of Equation 41 both scale as G^3 while the last two terms scale as G . For $|G| \gg 1$ the first two terms dominate, and balancing these terms yields an ion drift wave $X = -G(1+H)$. This wave propagates in the electron diamagnetic direction for $H > -1$ and in the ion diamagnetic direction for $H < -1$.

Similarly, in the limit that X scales as G^0 , the second and fourth terms in Equation 41 are both linear in G while the first and third terms have no G -dependence. Balancing the second and fourth terms yields the two solutions $X = \pm\sqrt{\frac{-H}{1+H}}$. The conditions $H \leq -1$ and $0 < H$ are unstable in this limit. The asymptotic growth rate at large- $|G|$ is $\sqrt{\frac{H}{1+H}}$. This growth rate is independent of k_y/Ω_i and is of order unity, implying that the growth rate scales with the MHD growth rate.

In the case $H = -1$, the asymptotic behavior is found by assuming that X scales as $G^{1/3}$. Here the cubic term and the constant term balance. The three modes are $X = G^{1/3}$ and $X = G^{1/3}(-1/2 \pm i\sqrt{3}/2)$, and the growth rate of the unstable branch asymptotes to infinity.

The roots of the two-fluid dispersion relation (41) are calculated numerically in order to analyze the stability for arbitrary G and H . We plot the real and complex

roots as a function of G for given values of H . Increasing $|G|$ corresponds to increasing the Hall parameter for a fixed equilibrium.

The roots are shown in Figure 3 for the case where $H = 0$. This case is analogous to the Roberts-Taylor dispersion relation,⁴ but it includes a zero-frequency drift wave. The unstable g-mode and the corresponding stable branch are in green and blue respectively. Stabilization of the unstable branch is observed for $|G| \geq 2$. These two modes have a real frequency of $-G/2$ for $|G| < 2$. Their real frequencies split at $|G| = 2$. For large- G one frequency tends towards 0 and the other tends towards $-G$.

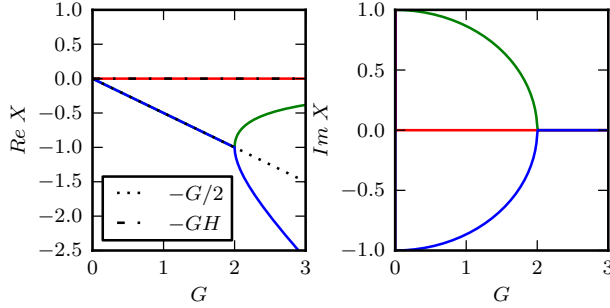


FIG. 3. The real and imaginary frequencies of the three modes are shown for $H=0$. The green line is the unstable g-mode, red is the drift wave, and blue is the stable branch. Stabilization occurs at $G^2 = 4$.

Similar behavior is observed for $-1/4 < H < 0$. Figure 4 shows the case for $H = -1/8$. Here, the two-fluid effects tend to stabilize the g-mode for all G . The green and blue lines correspond to the unstable and stable branches of the g-mode, and the red line is the drift wave. The drift wave has a finite frequency since $H \neq 0$. The drift wave and the two branches of the g-mode always propagate in opposite directions for $H < 0$. The critical- G at which stabilization is observed increases with decreasing H . Stabilization occurs at $|G| \approx 2.57$ for the case shown in Figure 4.

In the region $-1 < H < -1/4$, the analysis predicts that the two-fluid effects increase the growth rate of the unstable mode at small $|G|$, but stabilization is expected at large- $|G|$. Figure 5 shows the case for $H = -1/2$. The growth rate of the unstable g-mode increases for small values of $|G|$ and peaks around $|G| \approx 2.3$ with a maximum growth rate of $Im(X) \approx 1.1$. The growth rate decreases for $|G| > 2.3$, and stabilization occurs at $|G| \approx 6.67$. The maximum growth rate and critical- G required for stabilization increase with decreasing H . At $H = -1$ stabilization is lost, and for $H \leq -1$ the two fluid effects are destabilizing for all G . Figure 6 shows the case for $H = -3/2$ and is representative of all cases with $H < -1$. The maximum growth rate decreases as H is reduced below -1 . In the limit $G \rightarrow \pm\infty$ the asymptotic growth rate is $\sqrt{\frac{H}{H+1}}$.

Now consider conditions where $H > 0$. Figure 7 shows

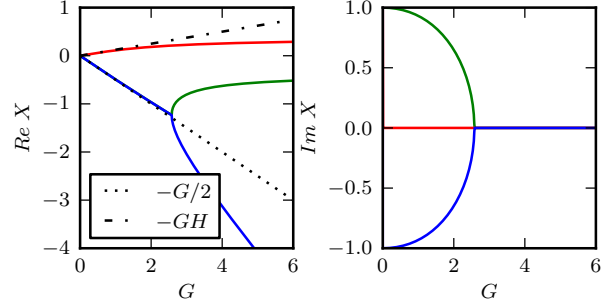


FIG. 4. The complex frequencies of the three modes are shown for $H = -1/8$. This case is representative of all cases with $-1/4 < H < 0$. Stabilization is observed for $|G| \gtrsim 2.57$. The ion drift wave has a finite real frequency. The g-mode and the ion drift wave propagate in opposite directions.

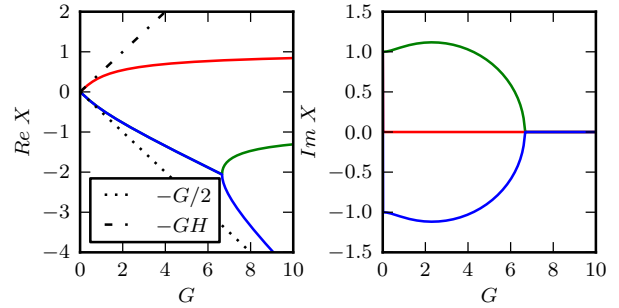


FIG. 5. The complex frequencies of the three modes are shown for $H = -1/2$. This case is representative of all cases with $-1 < H < -1/4$. The two-fluid effects increase the linear growth rate for small $|G|$. The two-fluid effects decrease the growth rate at sufficiently large $|G|$, and stabilization is observed.

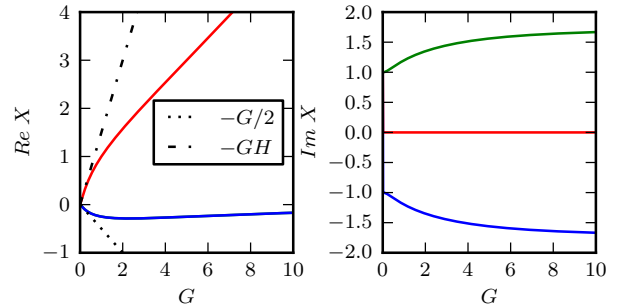


FIG. 6. The complex frequencies of the three modes are shown for $H = -3/2$. This case is representative of all cases with $H < -1$. There is no stabilization of the g-mode and the two-fluid effects increase the growth rate of the unstable mode for all G . For the case shown, the growth rate asymptotes to $\sqrt{3}$ as $|G| \rightarrow \infty$.

the case for $H = 0.04$. Here, the two-fluid effects tend to stabilize the g-mode for small- $|G|$, and stabilization occurs at $|G| \approx 1.85$. However, as $|G|$ is increased, a second mode becomes unstable at $G \approx 2.55$. For $H > 0$ the

drift wave and the two branches of the g-mode drift in the same direction in the plasma rest frame. At $|G| \approx 2.55$ the drift wave intercepts the low-frequency branch of the stabilized g-mode. Here the second instability becomes unstable. Like the g-mode, this second instability has a corresponding damped mode.

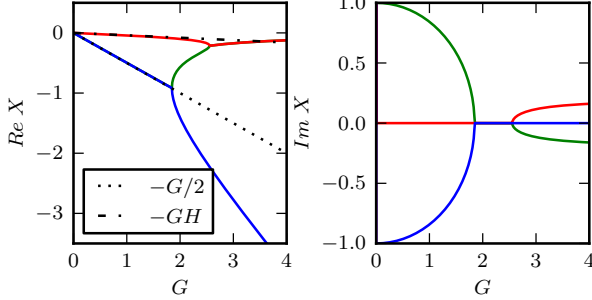


FIG. 7. The complex frequencies of the three modes are shown for $H = 0.04$. Stabilization of the g-mode occurs at $|G| \approx 1.85$. A second mode is destabilized at $|G| \approx 2.55$. The second mode becomes unstable when the drift wave intercepts the low-frequency branch of the stabilized g-mode. This new mode is unstable for all $|G| \gtrsim 2.55$ and has an asymptotic growth rate of 0.196.

As H is increased, the critical- G for stabilization of the g-mode decreases, and the critical- G for the onset of the second instability decreases. The width of the region of stability also decreases. At $H = 1/8$ these two points coincide, and stability only occurs at $|G| = \frac{8}{9}\sqrt{3}$. The case is shown in Figure 8. This point satisfies the equality relation in Equation 45. It also corresponds to where the drift wave intersects the g-mode at the point that the g-mode is stabilized. Here, both branches of the g-mode and the drift wave all have the same frequency.

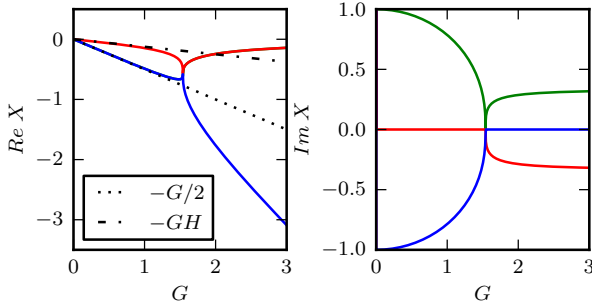


FIG. 8. The complex frequencies of the three modes are shown for $H = 1/8$. The ion-drift wave (red) intersects both branches of the g-mode (blue and green) at the point $|G| = \frac{8}{9}\sqrt{3}$. Here, the MHD g-mode is stabilized and the second mode simultaneously becomes unstable.

For $H > 1/8$ there is no region of stability along the entire G axis. A representative case is shown in Figure 9 for $H = 0.15$. For all positive H , the maximum growth rate is less than unity. The asymptotic growth rate as

$G \rightarrow \pm\infty$ is $\sqrt{\frac{H}{H+1}}$, and this asymptotic growth rate approaches 1 as H is increased.

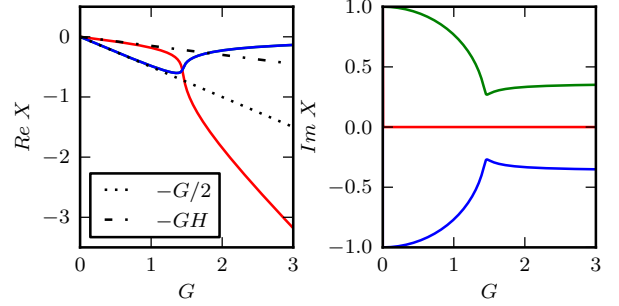


FIG. 9. The complex frequencies of the three modes are shown for $H = 0.15$. This case is representative of all cases with $H > 1/8$. Here the real frequency of the drift wave (red) intersects the real frequency of g-mode before the g-mode is stabilized. There is no region of stability.

In summary the two-fluid modifications of the g-mode are more complicated than the dynamics represented by the Roberts-Taylor dispersion relation: $\omega^2 + \omega_*\omega + \Gamma_{MHD}^2$.⁴ The stabilization properties represented in Equation 41 strongly depend on the parameter H , which only depends on the equilibrium ion pressure, density, and gravity. A dependence on temperature is implicit in the relation between pressure and density. The stability properties are summarized as follows. The g-mode is unstable for $H \leq -1$, and two-fluid effects enhance the growth rate of the unstable mode for all G . For $-1 < H < -1/4$, two-fluid effects enhance the growth rate at small $|G|$, but are stabilizing at large $|G|$. Stabilization is observed for sufficiently large $|G|$. Two-fluid effects are stabilizing for all G for $-1/4 \leq H \leq 0$, and stabilization always results at a sufficiently large values of $|G|$. For $0 < H \leq 1/8$ the two-fluid effects are stabilizing for small- $|G|$, and stabilization occurs for a range of G . However a second mode becomes unstable at large enough $|G|$. For $1/8 < H$ the two-fluid effects reduce the growth rate with respect to the MHD g-mode, but an unstable mode exists for all values of G .

A key result is the appearance of a second instability when H is positive. For $0 < H < 1/8$ this second instability forms when the drift wave interacts with the low-frequency branch of the stabilized g-mode. The two waves merge into a growing mode and a damped mode.

In terms of physical quantities the parameter H is

$$H = \frac{-p_i \frac{n'}{n} (\eta_i - (\gamma_s - 1))}{\rho g} \quad (46)$$

where $\eta_i = \frac{nT'}{n'T}$. The second expression relates H to the ion temperature gradient (ITG) stability parameter η_i . The condition of positive H corresponds to $\eta_i > 2/3$ for $\gamma_s = 5/3$ (the unstable g-mode requires $\frac{n'}{n}$ and g have opposite signs). The criterion that the second

mode is unstable ($\eta_i > 2/3$) is the same criterion for ITG instability.

Despite having the same stability criteria, there are a number of differences between the second instability and the ITG mode. The second mode is driven unstable by an interaction between the stable drift wave and the low-frequency branch of the g-mode. The ITG is a parallel sound wave that is driven unstable by an interaction with ion drifts.²⁴ The growth rate of the second mode scales with the growth rate of the MHD g-mode, whereas the growth rate of the ITG scales with the sound wave frequency. The ITG requires $k_{\parallel} \neq 0$, but our model (Equation 41) assumes $k_{\parallel} = 0$.

D. Analysis of the Full Extended MHD g-mode

We now analyze the full g-mode dispersion relation that includes both gyroviscosity and the two-fluid Ohm's law (Equations 14-21). The analysis first considers the limit $|G| \ll 1$ and then considers various large- $|G|$ limits. Finally, the solutions to Equation 14 are evaluated numerically.

Equations 25-27 describe the solution in the limit $|G| \ll 1$. Equation 25 produces the stable drift wave $X = -D_1/\Upsilon_0$. As is the case for the two-fluid model, the direction of propagation is determined by the sign of $P - \gamma_s N$. The wave propagates in the electron direction if $P > \gamma_s N$ and in the ion direction if $P < \gamma_s N$. Equations 26-27 describe the g-mode and the corresponding damped mode.

Now consider the limit of large $|G|$ and finite \sqrt{N} . The model is not physically valid in this limit as it violates $k_y r_i \ll 1$. However, this limit can be realized in small-scale dynamics of numerical codes that use the extended MHD model. The dispersion relation in this limit is

$$A_2 X^3 + X_{*3} X^2 + \Upsilon_2 X + D_1 = 0. \quad (47)$$

The three roots of the equation can be found using the orderings $X \sim G^1$ and $X \sim G^{-1}$. In the case where $X \sim G^1$ the first two terms dominate, and the approximate solution is

$$X \approx -\frac{X_{*3}}{A_2} + O(G^0) = \frac{GN}{\tau\beta} + O(G^0). \quad (48)$$

In the case where $X \sim G^{-1}$ the quadratic, linear, and constant terms dominate. The resulting solutions are

$$X \approx -\frac{\Upsilon_2}{2X_{*3}} \left(1 \mp \sqrt{1 - \frac{4D_1 X_{*3}}{\Upsilon_2^2}} \right) + O(|G|^{-2}). \quad (49)$$

The first mode is a drift wave that propagates in the ion direction. The second two modes limit to zero-frequency modes as $G \rightarrow \infty$. They are stable if $4D_1 X_{*3}/\Upsilon_2^2 < 1$. A sufficient condition for stability is $4D_1 X_{*3} =$

$G^4 N^2 (P - \gamma_s N) < 0$ or more simply $P < \gamma_s N$. The condition $P < \gamma_s N$ is equivalent to $\eta_i < 2/3$ for $\gamma_s = 5/3$. The ratio $4D_1 X_{*3}/\Upsilon_2^2$ is often small for realistic parameters, and there are many cases that are stable but violate the criteria $P < \gamma_s N$, so it does not represent a necessary condition for stability.

The above results are only valid if A_2 , X_{*3} , Υ_2 , and D_1 are all nonzero. The qualitative behavior of the model can change if any of these terms are zero. An interesting case to consider is $X_{*3} = 0$ and $\Upsilon_2 = 0$. The terms X_{*3} and Υ_2 represent the coupling between the two-fluid effects and gyroviscosity. They only appear when both effects are included in the model self-consistently. Neglecting these two terms is representative of simple models that account for two-fluid effects and gyroviscosity by adding their respective drifts.

When $X_{*3} = 0$ and $\Upsilon_2 = 0$, the dispersion relation is

$$A_2 X^3 + X_{*1} X^2 + \Upsilon_0 X + D_1 = 0. \quad (50)$$

The roots of the equation are found by using the ordering $X \sim G^{-1/3}$. Here the first and last terms balance, and to lowest order, the roots are

$$X = \left(\frac{-D_1}{A_2} \right)^{-1/3} \quad (51)$$

and

$$X = \left(\frac{-D_1}{A_2} \right)^{-1/3} \left(\frac{-1}{2} \pm \frac{\sqrt{3}}{2} i \right). \quad (52)$$

The first mode is a stable wave, and the other two solutions are an unstable mode and the corresponding stable mode. The growth rate of the unstable mode scales $G^{-1/3}$, and all three modes approach zero frequency as G approaches ∞ .

We calculate the roots of the full extended MHD dispersion relation numerically to investigate stability at intermediate values of G . We start by considering an equilibrium with $\beta = 1\%$, $\gamma_s = 5/3$, and $\tau_i = 1/2$. Figure 10 shows the maximum growth rate for $N = 10$ as a function of P and G . The color contours indicate the normalized growth rate, and white regions are stable. The horizontal line at $P = 10$ marks the point where $P = N$. Here, the equilibrium temperature gradient is zero. Below this line the temperature gradient opposes the density gradient, and above this line the two gradients point in the same direction. The vertical line at $G \approx 0.032$ marks the condition where $k_y r_i = 1/10$. The maximum value of G shown corresponds to $k_y r_i = 1/2$.

Stabilization of the g-mode does not occur for $k_y r_i < 1/2$ when $P \lesssim N$. It may occur at larger values of G , but here the extended MHD model is not valid. However, when $P > N$ there is a large region of stability at finite G . Often, when P is small, stability is not achieved until the validity of the extended MHD model is questionable;

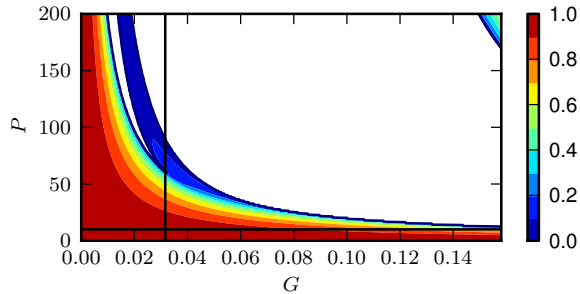


FIG. 10. Contours of constant $Im(X) > 0$ for the full model with $N = 10$ and $\beta = 1.0\%$. Regions of stability are white. The vertical line at $G \approx 0.032$ marks $k_y r_i = 1/10$ and the horizontal line marks $P = N$. The domain of G corresponds to $0 \leq k_y r_i \leq 0.5$.

however, at sufficiently large P stability occurs where extended MHD is valid. At sufficiently large P , there are three instabilities separated by two regions of stability.

The three roots of the dispersion relation are shown for $P = 100$ in Figures 11 and 12. Figure 11 focuses on the region around the g-mode and the second instability. The three modes are the unstable g-mode (green), its damped counterpart (blue) and an ion drift wave (red). All three modes propagate in the electron diamagnetic direction, and initially both branches of the g-mode have the same real frequency. At the point of stabilization, the two branches of the g-mode become real waves with distinct real frequencies. Then, the ion drift wave intersects the high-frequency branch, and this interaction creates a new instability. This new instability has a growth rate that is less than the MHD growth rate; it is stabilized at a large value of G , and after stabilization its two branches become real waves with distinct frequencies. Figure 12 shows that these two real waves recombine at an even larger value of G to produce a third instability. This third instability has a growth rate that is larger than the original MHD growth rate, but it exists in a region where extended MHD is not valid. The third instability has a maximum growth rate that is approximately 260 times larger than the MHD growth rate. It is eventually stabilized around $G = 4.0$ (not shown).

Between $P = 50$ and $P = 60$, the g-mode and second instability merge. Here, there is no region of stability separating the two modes. However, the interaction of the drift wave with the g-mode still has an effect. As illustrated in Figure 13, there is a noticeable bulge in the traces that extends the region of instability.

Results shown in Figure 10 are representative of the dynamics for a wide range of N and β . In general when $P \gg N$ there are at least three distinct instabilities. The first mode is the MHD g-mode, the second mode is driven by the interaction between the high-frequency branch of stabilized g-mode and the ion drift wave, and the third instability is a recombination two branches of the previously stabilized mode. As P is decreased, there is a

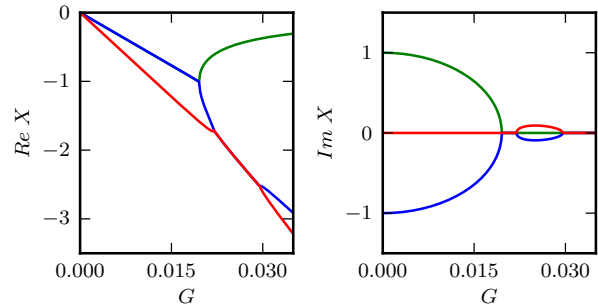


FIG. 11. Linear spectrum for the full model with $N = 10$, $P = 100$, and $\beta = 1.0\%$. Similar to the two-fluid model, there is a second instability that is driven unstable when the ion-drift wave interacts with the high-frequency branch of the stabilized g-mode.

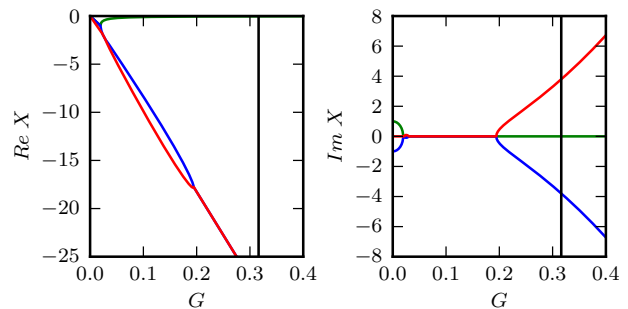


FIG. 12. The linear spectrum calculated using the full model using the same parameters as Figure 11. The domain is expanded to show the onset of the third instability. This mode is destabilized when the two stabilized branches on the second instability recombine.

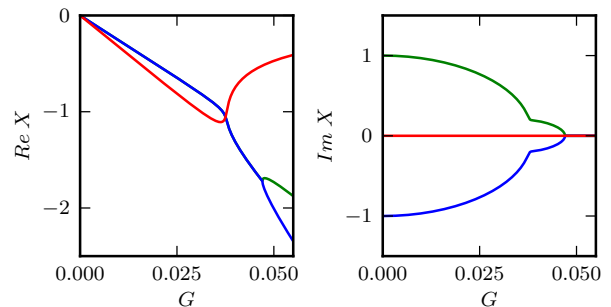


FIG. 13. The linear spectrum calculated using the full model with $N = 10$, $P = 50$, and $\beta = 1.0\%$. Here, there is no region of stability between the g-mode and the second mode. However, the second mode delays the onset of stability.

critical point where the g-mode and the second mode merge, and they are no longer distinguishable. This critical point increases with both N and β .

The second mode is similar to the mode observed in the two-fluid model in that they are both driven unstable by an interaction between the ion drift wave and one of the branches of the g-mode. However, there are some

qualitative differences in the results from the two models. In the two-fluid model, the mode is destabilized when the ion drift wave interacts with the low-frequency branch of the stabilized g-mode. At small positive H , the g-mode and this second mode are distinct modes, while at larger values of H , these two modes merge into one. Note that $H = P - \gamma_s N$, and increasing H corresponds to increasing P for fixed N . In the full model, the second mode is driven unstable by an interaction between the ion drift wave and the high-frequency branch of the stabilized g-mode. At small values of P , the g-mode and the second mode are indistinguishable, but at sufficiently large values of P , the two modes become distinct. In the two-fluid model, this second mode is unstable at $G = \infty$, while in the full model, the mode is stabilized at finite G .

The third instability is a concern for numerical codes, such as NIMROD, that use the extended MHD model. While this mode usually exists in a regime where extended MHD is not physically valid, it exists in the model. It may arise in computations that require highly resolved meshes. It has a maximum growth rate that greatly exceeds the MHD growth rate, so it may dominate an otherwise-resolved extended MHD simulation. While not universal, this mode is unstable for a wide range of P , N , and β .

Finally, there are cases at high- β that contain a fourth instability. This fourth instability exists at values of G that are greater than the third regime of the instability, and the extended MHD model is not valid. The growth rate of this fourth mode is less than the maximum growth rate of the third mode.

IV. LINEAR ANALYSIS OF STRAIGHT SPHEROMAK EQUILIBRIA

In this section we present extended MHD computations of interchange modes in cylindrical screw-pinch equilibria. The results exhibit many of the same qualitative features that are observed in the analysis of the g-mode. The screw-pinch equilibria have spheromak-like parameters, and we refer to them as “straight spheromaks.” The profiles are a generalization of those used by Jardin,¹⁶ where the pressure is calculated by specifying a uniform Suydam stability parameter across the domain. The resulting pressure gradient is given by the formula $\mu_0 p' = -D_s r \frac{B_z^2}{2} \left(\frac{q'}{q}\right)^2$, where $D_s = 0.25$ corresponds to ideal marginal stability. The equilibria use a quadratic safety factor profile, $q(r) = q_0 \left(1 - q_2 \frac{r^2}{a^2}\right)$, that allows for non-zero safety-factor values at the boundary, $r = a$, unlike reference 6. Also, unlike the slab configurations of Section III, these screw-pinch equilibria have magnetic shear. Our boundary conditions at $r = a$ represent a close-fitting, electrically conducting wall.

By generating a family of equilibria with D_s ranging from 0.2 to 2.0, we are able to study interchange modes that are resistively unstable, weakly ideally unsta-

ble, and strongly ideally unstable. A case with $D_s = 0.2$ is ideal-interchange stable but resistive-interchange unstable. It is slightly below the ideal marginal stability point of $D_s = 0.25$. The other cases with $D_s > 0.25$ are all ideal-interchange unstable. The equilibrium density and temperature profiles are calculated from the pressure. All the cases presented use uniform density; however, calculations that use uniform temperature for the same pressure profile exhibit similar behavior.¹³

The parameters of our straight-spheromak computations are based on conditions achieved in SSPX,¹⁵ where consistency of pressure profiles before and after MHD activity imply a pressure-driven limit.²⁵ We list the dimensional parameters in Table I. The values represent a region that is inside the separatrix of SSPX’s flux-core configuration. The range in sound gyro-radius, $\rho_s = C_s/\Omega_i$, of $7.1 \times 10^{-3} \leq \rho_s(0)/a \leq 1.5 \times 10^{-2}$ results with our above-described scan of D_s from 0.2 to 2.0. The ion skin depth value corresponds to a Hall parameter value of $\Lambda = d_i/a = (\tau_a \Omega_i)^{-1} = 0.13$. The magnetic diffusivity, η/μ_0 , is treated as an externally controlled parameter that is separate from the equilibrium temperature, and the range of values corresponds to varying the Lundquist number ($S = a^2 \mu_0/\eta \tau_A$) over the physically relevant range of $6.3 \times 10^3 \leq S \leq 6.3 \times 10^6$.

TABLE I. Physical parameters in our straight-spheromak computations.

Parameter	Value (MKS)
minor radius, a	0.25 m
column length, L	2.0 m
edge pressure, $p(a)$	400 Pa
edge temp., $T_e(a) = T_i(a)$	25 eV
particle density, n	$5.0 \times 10^{19} \text{ m}^{-3}$
central field, $B(0)$	0.5 T
ion mass (H), m_i	$1.7 \times 10^{-27} \text{ kg}$
ion skin depth, d_i	0.032 m
sound gyro-radius, $\rho_s(0)$	$1.8 \times 10^{-3} \text{ m} - 3.8 \times 10^{-3} \text{ m}$
Alfvén velocity, V_A	$1.5 \times 10^6 \text{ m/s}$
Alfvén time, $\tau_A = a/V_A$	$1.6 \times 10^{-7} \text{ s}$
magnetic diffusivity, η/μ_0	$0.063 \text{ m}^2/\text{s} - 63.0 \text{ m}^2/\text{s}$

The safety factor q and normalized parallel current, $\lambda a = \mu_0 a J_{||}/B$, profiles of our straight-spheromak equilibria are shown in Figure 14. The parallel current profile only depends on the safety factor profile and the physical dimensions of the cylinder. Both profiles are independent of D_s . The safety factor on the magnetic axis is specified to be $q(0) = 0.66$, and at the boundary it is $q(a) = 0.52$. These values are chosen such that the $q = 1/2$ and $q = 2/3$ surfaces are not in the domain,²⁶ and the lowest-order resonant surface in the domain is the $q = 3/5$ surface. Although q -profiles of flux-core spheromaks are non-monotonic, our chosen profile is similar to the central part of distributions that were achieved at least transiently in SSPX discharges, as shown in Fig. 4b of Ref. 25. The corresponding λa profile decreases radi-

ally outwards from the magnetic axis and is comparable to optimized SSPX profiles, such as the reconstruction shown in Fig. 7 of Ref. 26.

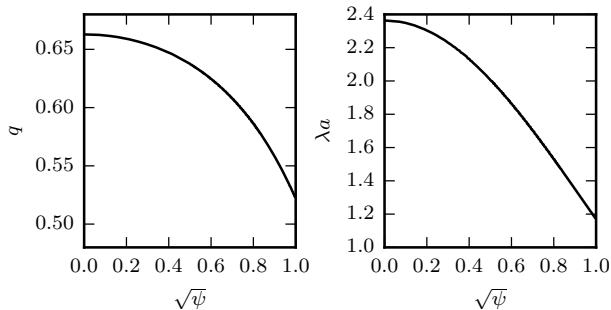


FIG. 14. Safety factor (q) and normalized parallel current density (λ_a) profiles for straight spheromak equilibria.

A characteristic ion diamagnetic frequency in our computations is calculated using $\omega_{*i} = \frac{m}{r_s} \frac{\Delta p_i}{aneB_0}$, where Δp_i is the change in the ion pressure from the magnetic axis to the wall, and r_s is the radius of the rational surface. The normalized ion diamagnetic frequency, $\omega_{*i}\tau_A$, for the $m = 3, n = 5$ mode resonant at the $q = 0.6$ surface varies from 4.3×10^{-4} for $D_s = 0.2$ to 4.3×10^{-3} for $D_s = 2.0$.

Our numerical computations use biquintic elements with a mesh of 40 elements in the radial direction and 20 elements in poloidal direction. The elements are radially packed near the mode rational surface. Sensitivity studies show that this spatial representation and the chosen time-step value for each computation yield linear growth rates accurate to 1%. For numerical reasons, all of our computations use small amounts of artificial density diffusion and thermal conduction. All computations in Sections IV A-IV C have the artificial number density hyperdiffusivity parameter set to $D_h = 1.7 \times 10^{-10} a^4 / \tau_A$. The isotropic thermal diffusivity χ_{iso} , number density diffusivity D_n , and viscosity ν_{iso} are varied with the magnetic diffusivity such that $\eta/\mu_0 = 10\nu_{iso}$, $\eta/\mu_0 = 10D_n$, and $\eta/\mu_0 = 100\chi_{iso}$. The magnetic divergence diffusivity is varied from 2.6×10^{-2} to 2.6 in a^2/τ_A , as needed, to maintain low divergence error without undue effect on the numerical eigenmodes.

A. Linear Resistive MHD Calculations

We start by considering interchange modes using the resistive MHD model as a baseline for comparison. Figure 15 shows the resistive MHD linear growth rates for the $m = 3, n = 5$ mode. Figure 15A shows the linear growth rates as a function of the Suydam parameter for $S = 6.3 \times 10^6$. The solid vertical line indicates the marginal ideal stability condition, $D_s = 0.25$. Near the marginal point, growth rates are small, $\gamma\tau_A = 0.016\%$ for $D_s = 0.5$, and the growth rate increases with increasing D_s . This is in agreement with the prediction that the growth rates are exponentially small near marginal

stability.^{27,28} Figure 15B shows the linear growth rate as a function of the resistivity. Resistive interchange scaling of $\gamma\tau_A \sim S^{-1/3}$ is observed for $D_s = 0.2$, consistent with expectation from analytical theory.²⁹ The cases with $D_s > 0.25$ behave ideally in that their growth rates do not scale with the resistivity, but they do increase with increasing D_s . We note that Ebrahimi, *et al.* previously studied the transition from resistive to ideal stability in cylindrical equilibria with shear.³⁰ Their profiles are relevant to reversed-field pinches, and the computations focus on $m = 1$ modes. Nonetheless, the two sets of findings are in qualitative agreement; for example, compare our Figures 15A-B to their Figures 2 and 4.

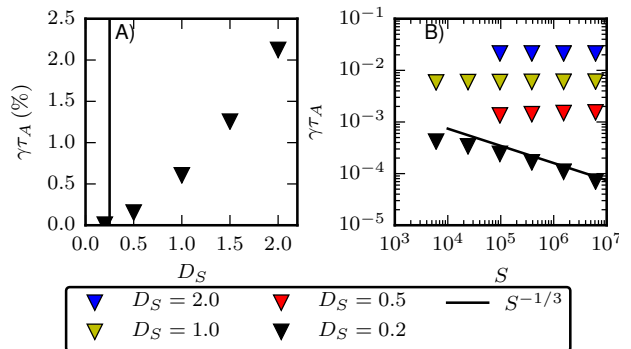


FIG. 15. The resistive MHD growth rates are plotted in A as a function of the Suydam parameter D_s for $S = 6.3 \times 10^6$. The vertical line indicates the ideal marginal stability point $D_s = 0.25$. The growth rates are plotted as a function of Lundquist number in B. The case $D_s = 0.2$ exhibits resistive interchange scaling.

B. Linear Calculations with Gyroviscosity

The linear calculations are repeated including ion gyroviscosity in the momentum equation, which is calculated self-consistently from the equilibrium. These calculations use the same physical and numerical parameters as the resistive MHD calculations. Figure 16 shows the linear growth rates and real frequencies calculated using this model. The growth rates are compared to the resistive MHD results in Figure 16A. We observe that gyroviscosity has a minimal effect on the growth rate of the strongly ideal unstable modes, i.e. $D_s \geq 1.0$. For the case with $D_s = 0.5$, gyroviscosity reduces the growth rate by 25% to 35%. For this case the growth rate is weakly dependent on S ; it changes by 7% as S is varied, but no clear trend is observed.

We find that the growth rate of the resistive mode, $D_s = 0.2$, scales as $\gamma\tau_A \sim S^{-2/5}$. This scaling is stronger than the resistive MHD scaling, $S^{-1/3}$, but not as strong as S^{-1} predicted for the limit $\omega_* \gg \gamma$.²⁸ Since the gyroviscous results show a stronger dependence on S than

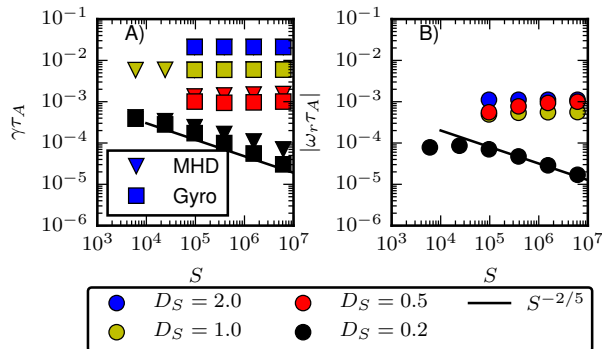


FIG. 16. The growth rates calculated using resistive MHD (triangles) and gyroviscous (squares) models are shown in A). The magnitude of the real frequency for the gyroviscous calculations are shown in B).

the resistive MHD results, gyroviscosity has more influence at large S . The growth rate is reduced by 7% at $S = 6.3 \times 10^3$, while the growth rate is reduced by 57% at $S = 6.3 \times 10^6$.

Gyroviscosity also imparts a real frequency on the modes. The magnitudes of these frequencies are shown in Figure 16B. The values are small compared to the growth rates for $D_s = 1.0$ and 2.0 , but they are comparable to the growth rates for $D_s = 0.2$ and 0.5 . The real frequency exhibits no dependence on S for $D_s = 2.0$, but it increases with S for $D_s = 0.5$ and 1.0 . For $D_s = 1.0$ the real frequency increases by 14% as S is increased from 9.6×10^4 to 6.3×10^6 . For $D_s = 0.5$ the real frequency increases by 80% over the same range in S . For $D_s = 0.2$ the real frequency decreases with increasing S . At large S -values the real frequency scales as $S^{-2/5}$, like the growth rate.

Figure 17 shows how the growth rate depends on the strength of the gyroviscosity for $D_s = 0.5$ and 0.2 . The vertical axes in Figures 17A-B use different scales. In these calculations the strength of the gyroviscosity is artificially scaled, and the Hall parameter, $\Lambda = d_i/a$, is used to indicate the strength of the gyroviscosity to make direct comparisons to calculations in Sections IV C and IV D that use the full extended MHD model. The growth rates in Figure 17 are calculated using $S = 1.6 \times 10^6$. The vertical lines indicate where the gyroviscosity has the correct magnitude for Equation 8, and the MHD limit without gyroviscosity is at $\Lambda = 0.0$.

We find that the growth rate always decreases with increasing Λ . However, there are two clear phases. At small Λ -values the growth rate has a strong dependence on Λ ; a small increase in Λ leads to a large decrease in the growth rate. In this region the real frequency of the mode increases with Λ . At large Λ -values the growth rate only weakly depends on Λ . Here, the real frequency slowly decreases with Λ . Similar behavior is observed for the $D_s = 1.0$ and $D_s = 2.0$ cases, but an unrealistically large gyroviscosity is needed to substantially affect the

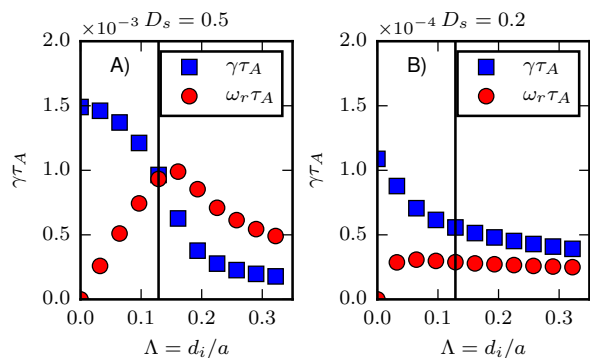


FIG. 17. The growth rate and real frequency, calculated using the gyroviscous model, as a function of the Hall parameter Λ for A) $D_s = 0.5$, B) $D_s = 0.2$. Calculations use $S = 1.6 \times 10^6$. The vertical line indicates the correct Hall parameter for these equilibria.

growth rate. Similar to the g-mode cases of Section III B with $X_{*g}^2 - 4A\Upsilon_0 < 0$, stabilization of the interchange mode through gyroviscosity alone is not observed for any of our straight-spheromak cases.

C. Single Temperature Extended MHD Calculations

We repeat the linear calculations using the full extended MHD model that includes the two-fluid Ohm's law and ion gyroviscosity in the momentum equation. These calculations solve a single temperature equation for T_i with T_e maintained at a fixed factor times T_i . Unless stated otherwise, we set $T_e = T_i$.

The computed growth rates for this model are shown in Figure 18. Unlike results from the gyroviscous model, the full extended MHD results are greater than the MHD growth rates for all D_s with $S \gtrsim 10^5$. The growth rate is increased by 65% for $D_s = 2.0$, and the growth rate is increased by approximately 20 – 25% for $D_s = 0.5$ and $D_s = 1.0$. The greatest difference is for $D_s = 0.2$ at the largest S -values. At $S = 6.3 \times 10^6$ the extended MHD growth rate is approximately seven times larger than the resistive MHD growth rate. Moreover, the extended MHD growth rate for $D_s = 0.2$ increases with increasing S , i.e. decreasing resistivity. The growth rate increases from $\gamma_{TA} = 4.0 \times 10^{-4}$ at $S = 9.6 \times 10^4$ to $\gamma_{TA} = 5.9 \times 10^{-4}$ at $S = 6.3 \times 10^6$, an increase of 48%. For this resistive case, $S \gtrsim 10^5$ is where the resistive skin-depth $d_\eta = \sqrt{a^2/S\gamma_{TA}}$ is comparable to or smaller than d_i .

Over most of the range of S -values shown in Figure 18, the real frequency of the modes is nearly independent of S for $D_s = 0.2, 1.0$, and 2.0 , and the magnitude of the frequency for these modes increases with D_s . However, the magnitude of the frequency for $D_s = 0.5$ is smaller than that for the $D_s = 0.2$ case, and the frequency dramatically decreases between $S = 9.6 \times 10^4$ and $S = 3.9 \times 10^5$.

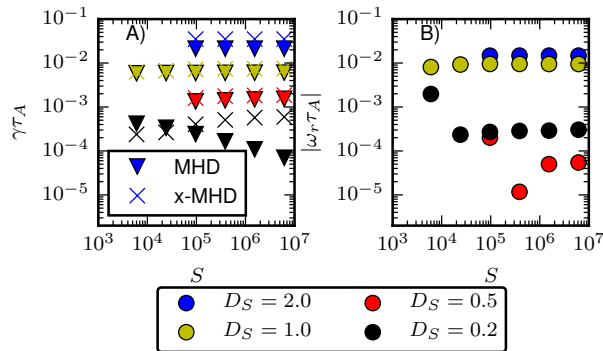


FIG. 18. The growth rate A) and real frequency B) as a function of S using the full extended MHD single temperature model. The extended MHD growth rates (x) are compared with the MHD growth rates (circles).

This large change in frequency is indicative of a transition to a different mode. A similar change in frequency is observed for $D_s = 0.2$ at small- S .

To understand this behavior we examine the dependence of the extended MHD growth rate when scaling Λ , as done in Section IV B. Figure 19 shows the growth rate at $S = 9.6 \times 10^4$. Here, there is evidence of two (or more) instabilities, and the one that dominates differs among different Λ -values. The extended MHD effects are stabilizing at small- Λ for all of the cases with $D_s \leq 1.0$, and the growth rate decreases with increasing Λ .

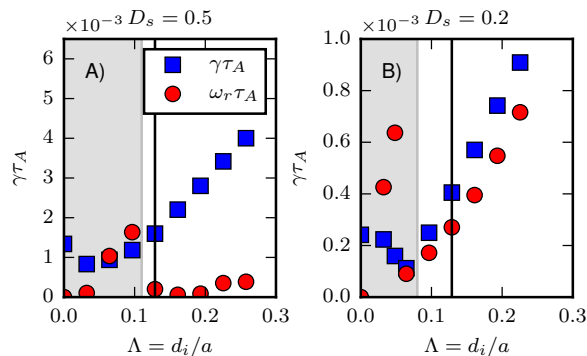


FIG. 19. The extended MHD growth rates and real frequencies are shown as a function of Λ for $S = 9.6 \times 10^4$.

A transition to a second instability is evident where the growth rate starts to increase with Λ . This transition occurs at $\Lambda \approx 0.06$ for $D_s = 0.2$, $\Lambda \approx 0.03$ for $D_s = 0.5$, and $\Lambda \approx 0.06$ for $D_s = 1.0$ (not shown). There is also a noticeable jump in the real frequency around this transition for $D_s = 0.2$ and $D_s = 0.5$. The real frequency for $D_s = 0.5$ jumps again between $\Lambda = 0.10$ and $\Lambda = 0.13$, possibly indicating a third mode, though the growth rate changes smoothly between these two values. The approximate range of Λ over which the extended MHD effects enhance stability relative to resistive MHD is indicated

by the shaded regions in Figures 19A-B. Thus, the physically relevant value of the Hall parameter (indicated by the black vertical lines) lies outside the region where the extended MHD effects improve stability. Here, the second instability is the dominant mode. Computed growth rates exhibit a similar dependence on Λ at $S = 1.5 \times 10^6$ (not shown). This is consistent with the results in Figure 18, which show that growth rates and, to a large extent, real frequencies do not change between $S = 9.6 \times 10^4$ and $S = 1.5 \times 10^6$.

The existence of the second instability counteracts the drift stabilization of the interchange mode. DeLucia, *et al.* did not observe a second instability in their two-fluid calculations,¹⁷ but they assumed cold ions, so the total pressure in their calculations is entirely due to the electrons. Motivated by the difference between the two results, we perform a second series of calculations where the electron temperature is three times the ion temperature. These computations have the same profile of total pressure as those with $T_e = T_i$. The results are shown in Figure 20 for $D_s = 1.0$ and $D_s = 2.0$. There is little change in the growth rate for $\Lambda \lesssim 0.05$, where the interchange mode is the dominant mode. However, at larger values of Λ , where the second instability dominates, the case with the colder ions has smaller growth rates. This trend is consistent with the differences between our results and the ($T_i = 0$) results of DeLucia, *et al.* It is also consistent with our “two-fluid,” i.e. extended MHD without ion FLR effects, analysis of the g-mode, discussed in Section III, which shows that the second instability does not exist in the cold-ion limit, where $H \rightarrow 0$.

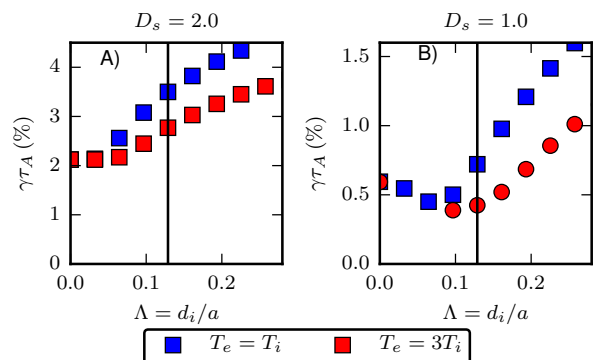


FIG. 20. Increasing the ratio of T_e/T_i decreases the linear growth rate at large Λ . The linear growth rates are shown for two values of T_e/T_i . These calculation use the single temperature extended MHD model at $S = 9.6 \times 10^4$.

D. Linear Extended MHD Two-Temperature Calculations

A model that is not considered in Section III includes gyroviscosity, the two-fluid Ohm’s law, and independent evolution of electron and ion temperatures. The equilibrium ion and electron temperatures profiles are assumed

to be equal, and we impose the ion-diamagnetic flow as part of the equilibrium. The calculations also include the diamagnetic heat flux density²⁰ $\vec{q}_* = -k_{*s} \hat{b} \times \nabla T_s$, where $k_{*i} = -\frac{5nT_i}{2m_i\Omega_i}$ and $k_{*e} = \frac{5nT_e}{2m_e\Omega_e}$. The diamagnetic heat flux is a FLR correction that is similar to gyroviscosity. However, the electron and ion diamagnetic heat fluxes cancel when $T_i = T_e$.

This model is the most computationally challenging model for NIMROD's combination of numerical methods, and the computations presented here use increased particle and thermal diffusivities. In these calculations we only consider $S = 9.6 \times 10^4$ and use $D_n = \chi_{iso} = 7\eta/\mu_0$. The isotropic viscosity is kept small relative to the magnetic diffusivity $\eta/\mu_0 = 10\nu_{iso}$.

The linear growth rates are calculated as a function of Λ by scaling the unit charge (e). The equilibrium ion flow is scaled consistently with the unit charge. The linear growth rates and their real frequencies are shown in Figure 21. Figure 21A shows the growth rate and real frequency for $D_s = 2.0$, and Figure 21B shows the growth rate and real frequency for $D_s = 1.0$. The shaded region roughly indicates the range of Λ where the extended MHD two-temperature growth rate is smaller than the resistive MHD growth rate. The solid vertical line indicates the physical value of Λ .

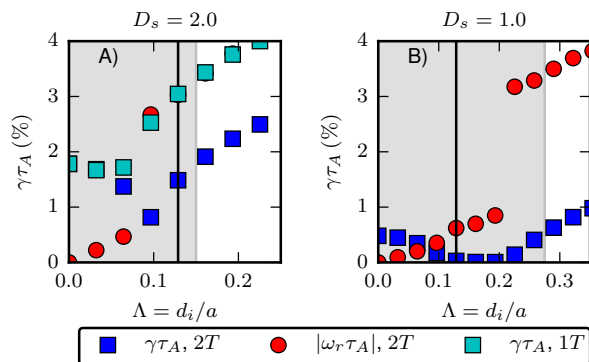


FIG. 21. The linear growth rates and real frequencies calculated using the full extended MHD model with separate electron and ion temperature advances are shown for $D_s = 2.0$ (A) and $D_s = 1.0$ (B). Also shown in A are the linear growth rates calculated using the single temperature full extended MHD model.

The enhanced particle and thermal diffusivities have a noticeable stabilizing effect on the MHD growth rate ($\Lambda = 0$). At $D_s = 2.0$ the enhanced diffusivities decrease the MHD growth rate by 16%. At $D_s = 0.2$ they decrease the MHD growth rate by 42%. For purposes of making direct comparisons, a series of extended MHD single-temperature calculations is rerun at $D_s = 2.0$ with the dissipation parameters used in the two-temperature computations. The results of these single-temperature calculations are also shown in Figure 21A.

The results of the $D_s = 1.0$ series of computations, shown Figure 21B, clearly indicate two separate insta-

stabilities. The interchange mode exists at small Λ -values, and its growth rate is reduced with increasing Λ . The real frequency of the mode increases roughly linearly with Λ . At $\Lambda = 0.13$ the interchange mode is nearly stabilized. The growth rate value of $\gamma\tau_A = 2.7 \times 10^{-4}$ represents a 94% reduction relative to the MHD limit. Between $\Lambda = 0.13$ and $\Lambda = 0.20$, the growth rate remains small and decreases with Λ , but the real frequency continues to increase linearly with Λ . Around $\Lambda = 0.2$ a second mode becomes unstable, as indicated by the jump in the real frequency. The growth rate and real frequency of the second mode increases with Λ , and its growth rate surpasses that of the MHD limit at $\Lambda = 0.27$.

Similar behavior can be observed for $D_s = 2.0$ in Figure 21A. However, the second instability becomes dominant before the extended MHD effects have significant influence on the interchange mode. The minimum recorded growth rate at $\Lambda = 0.09$ is 46% of the MHD limit, and a jump in the real frequency is observed between $\Lambda = 0.06$ and $\Lambda = 0.09$. We note that the transition to the second mode occurs at larger Λ -value for the two-temperature calculations than it does for the single-temperature calculations, and the two-temperature calculations yield appreciably smaller growth rates for all $\Lambda > 0.05$.

The extended MHD two-temperature model also reduces the interchange growth rate in $\Lambda < 0.2$ computations with $D_s = 0.2$ and $D_s = 0.5$. Moreover, the second instability is not observed in these conditions. Results presented in Ref. 13 show a particularly dramatic effect on the $D_s = 0.5$ mode, starting from modest Λ -values. The growth rates from the extended MHD two-temperature model are reduced by at least an order of magnitude relative to results with all other models, and the growth-rate values are comparable to those of resistive MHD interchange modes; for $0.03 \lesssim \Lambda < 0.2$ the growth rate is reduced to $\gamma\tau_A \approx 10^{-4}$. We note that for $D_s = 0.5$, the pressure gradient is substantial, leading to appreciable diamagnetic drifts, but the Suydam criterion remains in the small ideal growth-rate regime.²⁸

V. DISCUSSION AND CONCLUSIONS

In this study, we have analyzed two different classes of interchange-type modes with different extended MHD models that have been applied in a variety of contexts. Our g-mode analysis considers three different extended MHD models. The first two models are incomplete representations of the third model, which includes gyroviscosity and two-fluid effects. This third model is also incomplete in that it neglects the diamagnetic heat flux. Our straight-spheromak analysis also considers three different extended MHD models; though, we compare single- and two-temperature results and skip the model without gyroviscous stress. Although their physical relevance is limited, the simplified models can test different aspects of numerical models and are useful for verifying implementations.

Our first finding is that the three models have qualitatively different stability properties. The gyroviscous model is always more stable than MHD, and increasing the drift parameter $|G|$ always reduces the growth rate. There is only one instability in this model, the g-mode, but there are situations where stabilization fails, consistent with results from Ref. 7. The stability of the two-fluid model without gyroviscosity is determined by a balance between drifts due to equilibrium ion density and ion temperature gradients. This balance is characterized by the ITG stability parameter η_i ; a second instability exists when $\eta_i > 2/3$. This mode is driven unstable through the interaction of the ion drift wave and the low-frequency branch of the stabilized g-mode. For values of η_i near $2/3$, there is a stable region in G that separates the g-mode and the second instability. However, at sufficiently large η_i the two modes merge, and the region of stability disappears. This second mode grows at a rate that is comparable to the MHD g-mode, and it is unstable at infinite $|G|$.

A second mode is also observed in the full model, but there are qualitative differences between it and the second mode of the two-fluid model. In the full model, this instability is driven unstable through the interaction of the ion drift wave and the high-frequency branch of the stabilized g-mode. Where this mode initially appears in parameter space, there is no region of stability separating it from the g-mode. However, at sufficiently large η_i , the two modes are distinct and separated by a region of stability. This second mode is stabilized at finite G .

The dynamics of all three models is strongly influenced by ion drifts. The quantities N and P have factors of τ implicit in their definitions. (Note that the τ dependence in $S = \tau\beta/N$ is artificial.) In the cold-ion limit, the g-mode dispersion relation greatly simplifies:

$$(1 + \gamma_s\beta)\omega^2 + \omega_g\omega + \Gamma_M^2(1 + \gamma_s\beta) + \frac{g^2}{V_a^2} = 0. \quad (53)$$

This is the cold ion limit of the Roberts-Taylor dispersion relation, corrected for finite compressibility. Here, stabilization always occurs when ω_g is significantly large.

Our second finding is that the full extended MHD model produces unstable modes at $k_y r_i \gg 1$, where the small Larmor radius assumption is not valid. These instabilities have growth rates that are much greater than the MHD growth rate of the g-mode, and they may appear in computations that use extended MHD models which are based on small Larmor radius expansions. While such models can represent arbitrary magnetization due to collisional effects,^{20,31} kinetic treatments are needed to describe arbitrary orderings of spatial scales and gyroradii. This is the approach taken in Ref. 32, which reproduces the instability of the large Larmor radius fluid model from Refs. 10 and 11 in the “large g,” “cold ion” limit for collisionless conditions. It is possible that physical effects like the g-mode/magnetoacoustic wave coupling would drive instabilities at large $k_y r_i$ in small Larmor radius models, but the resulting modes are

likely distorted from the physically correct behavior by the incorrect ion-closure modeling.

Our general findings on the different stability properties of the three extended MHD models are qualitatively consistent with the results reported in Ref. 12. Direct comparison of our results and most of their local-analysis results is challenged by differences in equilibrium profiles. However, the $\beta = 0.1$ case shown in their Fig. 6 has little or no gradient in equilibrium- B , as in our profiles, since their $\beta p'$ approximately matches their Lgn/V_{Ac}^2 -value. Stabilization is achieved where the frequency is approximately equal to the growth rate in the $k \rightarrow 0$ limit, which is consistent with our result shown in Figure 1. However, we note that the two results are evaluated for different $S = g^2/V_a^2\Gamma_M^2$ values.

Our computations for straight-spheromak equilibria also show qualitatively different results for different extended MHD models. The gyroviscous model always produces growth rates that are smaller than MHD results, but the difference is only significant for $D_s \lesssim 0.5$. A second instability is present in the single-temperature extended MHD model that includes gyroviscosity and the two-fluid Ohm’s law. This second mode is unstable at experimentally relevant Λ -values and has a growth rate that is comparable to the resistive MHD growth rate. According to this model, the second instability is the dominant mode at SSPX-relevant values of Λ , and its growth rate is often greater than the MHD interchange growth rate. The instability also results with the two-temperature extended MHD model. However, the growth rate of the second instability is reduced, and the onset of the second instability occurs at larger Λ -values. As a result, there is a range of SSPX-relevant parameters with physical values of Λ and $D_s \lesssim 1.0$, where growth rates are significantly reduced relative to MHD predictions. This finding may be relevant to the apparent ideal-MHD β -limit observed in SSPX discharges during periods when the safety-factor profile lies above $1/2$.²⁵ A tendency for symmetry-breaking modes and reduced confinement in nonlinear resistive-MHD simulations of the quiescent phase of SSPX discharges has been noted in previous work,³³ and it is possible that consistent two-temperature extended MHD modeling would yield results that better represent the experiment’s confinement properties.

There have been other studies of extended MHD effects on resistive interchange modes that use this or similar equilibria. DeLucia *et al.* used this family of equilibria to study $m = 1$ interchange modes for $D_s = 0.175$.¹⁷ They found stabilization of these modes for $\Lambda \gtrsim 0.2$, and they do not encounter a second instability. However, they use a single-temperature two-fluid model that assumes cold ions. Hammet and Tang also studied resistive interchange modes in these equilibria using a gyrokinetic ballooning model.¹⁸ They order drift waves out of the system in their analysis. If the instability in the straight spheromak is due to a drift-wave interaction, as in the slab configuration, then the absence of ion drift

waves in these previous spheromak studies may explain why neither observe the second instability.

There are both similarities and differences between our g-mode results and those for the pressure-driven interchange in a screw pinch. The growth rate and frequencies calculated using the gyroviscous model are similar. For example, compare Figures 2 and 17. In both analyses the gyroviscous model is more stable than MHD, increasing the Hall parameter decreases the growth rate, and similar variations in the real frequency result.

A second instability is present in both the straight-spheromak and g-mode analyses when using the full extended MHD model. However, the growth rate of the second mode exceeds the MHD growth rate in the straight spheromak, whereas the resulting g-mode growth rate is always less than the MHD growth rate. Both analyses exhibit cases where there is a clear separation between the two modes, and both exhibit cases that smoothly transition from one mode to the other. In the straight-spheromak configuration, decreasing the ion temperature at fixed pressure decreases the growth rate of the second mode. For the g-mode decreasing the ion temperature delays the onset of the second mode and reduces its growth rate. Our complete eigenmode analysis for the slab equilibria shows that the second instability is due to an interaction between an ion drift wave and the g-mode. Our straight-spheromak computations only identify the fastest-growing mode for a given set of parameters, but the similarities in the results for the two configurations suggest that the second instability in the straight spheromak could be due to a similar interaction.

ACKNOWLEDGMENTS

The authors would like to thank Profs. C. Hegna and P. Zhu for informative discussion relevant to this work. This work was supported by the U.S. Department of Energy, Office of Science, Fusion Energy Sciences, under Award Numbers DE-FG02-06ER54850, DE-FC02-05ER54813, and DE-FC02-08ER54975.

Appendix A: Proof of Gyroviscous Stabilization for $P \geq N$.

In this appendix we show that the bracketed term in Equation 34 is positive for $0 < N \leq P$. Let the functions $U(P, N) = (aP + b)^2 - cN - d$ and $V(P) = (aP + b)^2 - cP - d$ where $a = (1 + \gamma_s \beta)(1 + \beta)$, $b = (2 + \gamma_s \beta)\tau\beta$, $c = \tau\beta(1 + \gamma_s \beta)$, and $d = \tau^2\beta^2$. The function U is the bracketed term in Equation 34, multiplied by $(1 + \gamma_s \beta + \frac{\tau\beta}{N})$. Positive U implies that the bracketed term is positive. The function V is the limiting case of U where $P = N$.

The difference between the two functions is $U(P, N) - V(P) = -c(N - P)$. By assumption $N \leq P$ and thus $U(P, N) - V(P) \geq 0$. Therefore if V is positive for

positive P , then U is positive for $0 < N \leq P$. V is a quadratic in P , and it has a global minimum at

$$P_{min} = \frac{\tau\beta}{2} \frac{1 - 2(2 + \gamma\beta)(1 + \beta)}{2(1 + \gamma\beta)(1 + \beta)^2} \leq 0. \quad (A1)$$

It is sufficient to evaluate $V(P = 0)$ since P_{min} is negative:

$$V(0) = b^2 - d = \tau^2\beta^2(3 + 4\gamma_s\beta + \gamma_s^2\beta^2) \geq 0. \quad (A2)$$

The proof is complete.

- ¹D. D. Schnack, D. C. Barnes, D. P. Brennan, C. C. Hegna, E. Held, C. C. Kim, S. E. Kruger, A. Y. Pankin, and C. R. Sovinec, *Physics of Plasmas* **13**, 058103 (2006).
- ²J. P. Freidberg, *Reviews of Modern Physics* **54**, 801 (1982).
- ³M. N. Rosenbluth, N. A. Krall, and N. Rostoker, *Nucl. Fusion Suppl.* **1**, 143 (1962).
- ⁴K. V. Roberts and J. B. Taylor, *Physical Review Letters* **8**, 197 (1962).
- ⁵J. D. Huba, *Physics of Plasmas* **3**, 2523 (1996).
- ⁶N. M. Ferraro and S. C. Jardin, *Physics of Plasmas* **13**, 092101 (2006).
- ⁷P. Zhu, D. D. Schnack, F. Ebrahimi, E. G. Zweibel, M. Suzuki, C. C. Hegna, and C. R. Sovinec, *Physical Review Letters* **101**, 085005 (2008).
- ⁸R. Goto, H. Miura, A. Ito, M. Sato, and T. Hatori, *Physics of Plasmas* **22**, 032115 (2015).
- ⁹B. H. Ripin, E. A. McLean, C. K. Manka, C. Pawley, J. A. Stamper, T. A. Peyser, A. N. Mostovych, J. Grun, A. B. Hassam, and J. Huba, *Physical Review Letters* **59**, 2299 (1987).
- ¹⁰J. D. Huba, J. G. Lyon, and A. B. Hassam, *Physical Review Letters* **59**, 2971 (1987).
- ¹¹A. B. Hassam and J. D. Huba, *Physics of Fluids* **31**, 318 (1988).
- ¹²A. Ito and H. Miura, *Physics of Plasmas* **23**, 122123 (2016).
- ¹³E. C. Howell, *Extended MHD Study of Interchange Modes in Spheromaks*, Ph.D. thesis, University of Wisconsin-Madison (2015).
- ¹⁴E. B. Hooper, L. D. Pearlstein, and R. H. Bulmer, *Nuclear Fusion* **39**, 863 (1999).
- ¹⁵E. B. Hooper, R. H. Bulmer, B. I. Cohen, D. N. Hill, C. T. Holcomb, B. Hudson, H. S. McLean, L. D. Pearlstein, C. A. Romero-Talamás, C. R. Sovinec, B. W. Stallard, R. D. Wood, and S. Woodruff, *Plasma Physics and Controlled Fusion* **54**, 113001 (2012).
- ¹⁶S. Jardin, *Nuclear Fusion* **22**, 629 (1982).
- ¹⁷J. DeLucia, S. C. Jardin, and A. H. Glasser, *Physics of Fluids* **27**, 1470 (1984).
- ¹⁸G. Hammett and W. Tang, *Nuclear Fusion* **23**, 1503 (1983).
- ¹⁹T. Nicolas and K. Ichiguchi, *Nuclear Fusion* **56**, 026008 (2016).
- ²⁰S. I. Braginskii, *Reviews of Plasma Physics* **1**, 205 (1965).
- ²¹R. D. Hazeltine and J. D. Meiss, *Plasma Confinement* (Addison-Wesley, Redwood City, CA, 1992).
- ²²C. R. Sovinec, A. H. Glasser, T. A. Gianakon, D. C. Barnes, R. A. Nebel, S. E. Kruger, D. D. Schnack, S. J. Plimpton, A. Tarditi, M. S. Chu, and the NIMROD Team, *Journal of Computational Physics* **195**, 355 (2004).
- ²³C. R. Sovinec, J. R. King, and the NIMROD Team, *Journal of Computational Physics* **229**, 5803 (2010).
- ²⁴D. D. Schnack, J. Cheng, D. C. Barnes, and S. E. Parker, *Physics of Plasmas* (1994-present) **20**, 062106 (2013).
- ²⁵S. Woodruff, E. B. Hooper, L. D. Pearlstein, R. Bulmer, D. N. Hill, C. T. Holcomb, H. S. McLean, J. Moller, B. W. Stallard, and R. D. Wood, *Physics of Plasmas* **13**, 044506 (2006).
- ²⁶H. S. McLean, R. D. Wood, B. I. Cohen, E. B. Hooper, D. N. Hill, J. M. Moller, C. Romero-Talamás, and S. Woodruff, *Physics of Plasmas* **13**, 056105 (2006).
- ²⁷T. E. Stringer, *Nuclear Fusion* **15**, 125 (1975).

- ²⁸S. Gupta, J. D. Callen, and C. C. Hegna, *Physics of Plasmas* **9**, 3395 (2002).
- ²⁹B. Coppi, J. M. Greene, and J. L. Johnson, *Nuclear Fusion* **6**, 101 (1966).
- ³⁰F. Ebrahimi, S. C. Prager, and C. R. Sovinec, *Physics of Plasmas* (1994-present) **9**, 2470 (2002).
- ³¹J.-Y. Ji and E. D. Held, *Physics of Plasmas* **20**, 042114 (2013).
- ³²J. D. Huba, A. B. Hassam, and D. Winske, *Physics of Fluids B* **2**, 1676 (1990).
- ³³E. B. Hooper, B. I. Cohen, H. S. McLean, R. D. Wood, C. A. Romero-Talamás, and C. R. Sovinec, *Physics of Plasmas* **15**, 032502 (2008).